CHARGE EXCHANGE REACTION RATE EVALUATION FOR DIFFERENT IMPURITIES AT MODERATE TEMPERATURES

Julia Pérez González

Tutored by

Dr. Eleonora Viezzer

Bachelor in Physics. University of Sevilla. Departamento de Física Atómica, Molecular y Nuclear.

Sevilla, July, 2023

Acknowledgements

Comenzar agradeciendo a Eli y a Diego la oportunidad de realizar el TFG con ellos y de ayudarme en cada paso del proceso. Sobre todo a Diego, por estar siempre pendiente de cada duda que me surgiese y listo para ayudar. Gracias

A mi familia. Por no dejar de apoyarme en ningún momento y por inculcarme desde pequeña las ganas de aprender. Gracias por enseñarme desde muy niña el valor del esfuerzo, la dedicación y el estudio. Y por soportar alguna que otra queja a la que siempre me respondían bromeando "deberías haber hecho filología inglesa".

Y a mis amigas y amigos. Por el apoyo incondicional y los miles de recuerdos. La horas de biblioteca pasaron a ser divertidas. Y a todas la personas que he conocido estos años. Habeis hecho los momentos más duros de la carrera mucho más llevaderos. Gracias por el compañerismo y las continuas ganas de querer ayudarnos unos a otros.

Thank you to everyone that during these years left a piece of them on the way. "Thank you in many different languages"

Contents

English Abstract

This bachelor thesis is dedicated to the Gas Puff-Charge Exchange Recombination Spectroscopy (GP-CXRS), a spectroscopy diagnostic that provides information on different parameters in a plasma such as the impurity ion temperature, rotation and density along the viewing lines of sight (LOS). The method consists in the injection of a thermal neutral gas in the plasma. The neutrals experience a charge-exchange reaction leading to a transfer of one electron to an impurity ion. As the impurity ion is now in an excited state, it will decay to a lower energy state emitting a characteristic photon. This is, a characteristic radiation that can be measured in the form of spectroscopy.

As for impurity ion density, charge exchange effective emission rates are needed, a code written in Python is developed in order to calculate those rates from raw CXRS cross-sections. The cross-sections for every studied CXRS reaction are taken from the database OpenAdas. Different effects in the charge exchange (CX) reaction must be considered: nl-cascade and l-mixing effects. The objective is to have a code that can then be used to study any CXRS reaction. Thus, the final results will be first compared with the ones obtained by [1] to make sure that the code performs as expected. Moreover, a suitable reaction for CXRS at the SMART tokamak of the University of Sevilla will be identified.

List of used acronyms

- CXRS (Charge eXchange Recombination Spectroscopy)
- GP (Gas puff)
- LOS (Lines Of Sight)
- JET Tokamak (Joint European Torus Tokamak)
- SMART (SMall Aspect Ratio Tokamak)
- ASDEX (Axially Symmetric Divertor Experiment)
- NBI (Neutral Beam Injection)
- ELMs (Edge Localized Modes)
- GP-CXRS (Gas puff-Charge eXchange Recombination Spectroscopy)
- CX (Charge eXchange)
- ADAS (Atomic Data and Analysis Structure)

1 Introduction

Since the very beginning of human history, energy has been a key factor in our evolution as a society. From what is known to be the first energy source ever used by humans: fire, to our current mostly fossil fuels-based energetic model, we have been in a constant search for affordable and efficient energy sources to make our world work. Paradoxically, it is this aim for productivity and efficiency that is asphyxiating our planet. Fossil fuels such as coal, oil or gas do strongly contaminate by emitting CO_2 and many other residues that are both toxic for the Earth and for every living creature [2]. Figure 1.1 shows the emissions of CO_2 of every respective fossil fuel source and other polluting industries over the last two centuries.

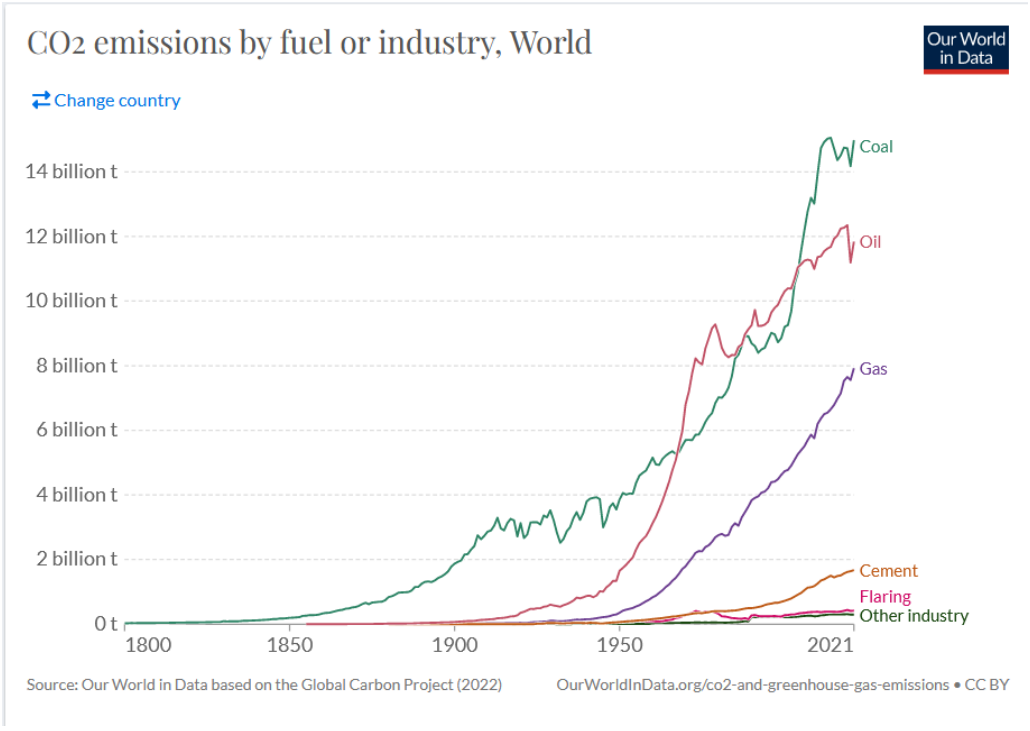

Figure 1.1: CO_2 emissions per fossil fuel and industry from 1800 to 2021. Source: [3].

Over more, energy resources are not equally distributed around the globe. This leads to a constant dependence of some countries on others. In fact, it is well known that energy has often been a matter of war and discomfort between territories in our most recent history and it is still now in the present. In addition to the environmental and social topic, a new issue appears: fossil fuels are not unlimited. According to recent studies, there is merely coal for no more than 139 years, oil for 54 and gas for approximately 49 [4].

If one looks at the demand for fossil fuels worldwide in the last century (figure 1.2), a slightly decrease in the previous decades can be noted. Indeed, at the beginning of the 40s, around 95% of the energy production was based on non-renewable energy sources. Meanwhile, now the same statistics for the year 2021 show a percentage of roughly 80%. Nuclear energy and the so-called renewable sources, such as solar, wind or hydro energy, to name a few, represent the rest of the production of worldwide energy in the recent years.

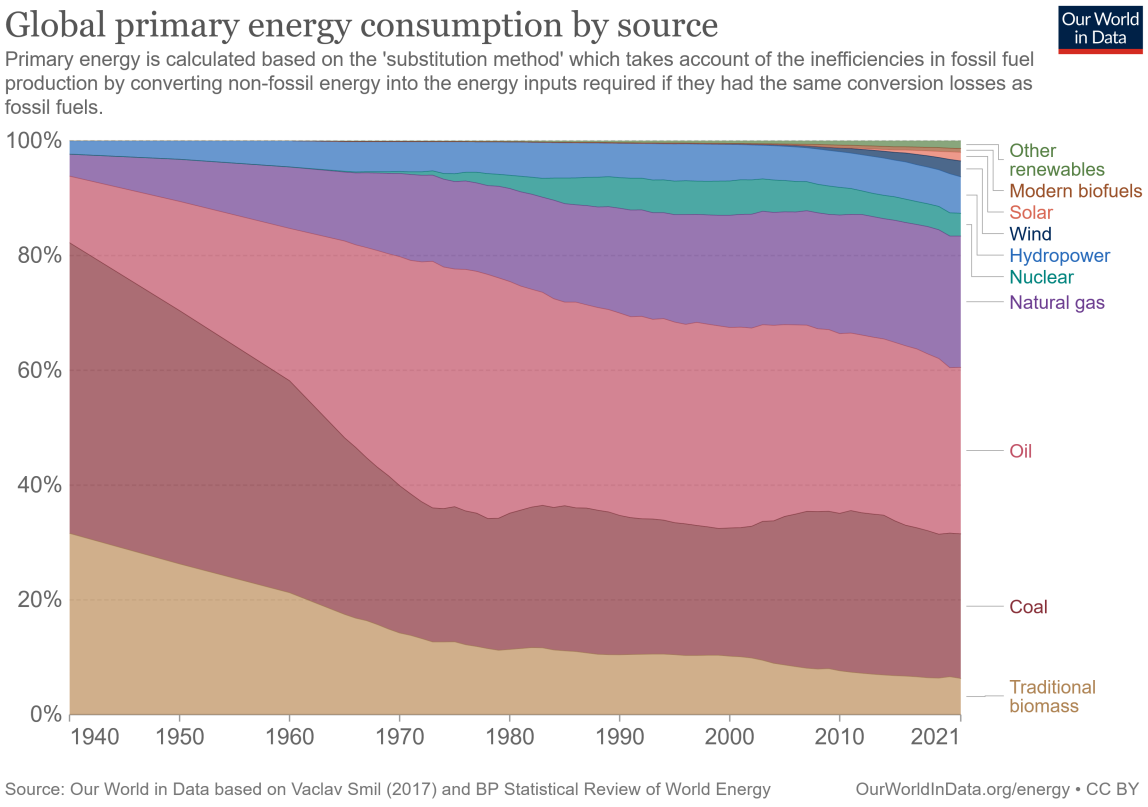

Figure 1.2: Global energy consumption from 1940 to 2021. Source: [5]

Nevertheless, these are definitely not good statistics regarding fossil fuels. We are still strongly dependent on non-renewable energy and so far, renewable ones are not a constant and stable source. This means a major problem for present and future generations and the planet itself.

Besides, a whole discussion about nuclear energy is the order of the day: whether to close nuclear power plants or not. These ones make use of nuclear fission reactors to produce energy. Notwithstanding, it is a fact that under controlled conditions, it is a safe and powerful energy source, many countries are considering ending nuclear energy production. In fact, Germany has already closed all of its nuclear power plants [6]. According to the current plan from the Spanish government, by 2035, nuclear plants must be closed as well in Spain [7]. This is being followed by many other European territories. It is undoubtedly a controversial topic due to the understandable fear of nuclear disasters. However, nuclear power plants are built and designed after decades of research and development to guarantee the minimum likelihood of an accident [8]. Furthermore, it does not produce contaminating gases and it is a constant and affordable energy source, being its energy ratio production-consumption very high [9]. We must accept, though, the radioactive waste released from nuclear fission is not a kind topic despite the security in the storing of these. We need then to think of a new way to produce enough energy for a world whose population and technology keep growing. A new source that is efficient, economical and overall clean and unlimited. Nuclear fusion is a promising candidate.

1.1 Nuclear fusion

By fusing two light nuclei, a heavier one is produced. As a result of the difference in mass between the initial and the final nuclei, a significant amount of energy is released recalling famous Einstein's equation: $E = mc^2$. This process is known as nuclear fusion. It occurs inside stars, and so it does as well in our sun. Thus, we can consider our main goal as building a sun on the Earth in order to provide virtually infinite energy to the whole world with zero residues. Yet, the process must be done differently, since the

conditions given in a star are totally others to the ones in our planet.

Before digging any further into this topic, two new concepts that play a great role in nuclear fusion shall be introduced. These are strong nuclear force and Coulombian interaction force, two of the elemental forces. For nuclear fusion to be induced, the mutual repulsion between the two nuclei due to their positive charges must be overcome. The strong nuclear force, on the contrary, is an attractive force that will allow fusion. Nonetheless, the strong force is only significant for distances of the order of $10^{-15}m$, which are nuclear distances. It would be necessary, then, to approach both nuclei such a distance.

Inside stars, the Coulombian force is overcome by proton-proton fusion, helium fusion or carbon cycle, depending on their mass and age. But all of them are under incredibly high temperatures. In the case of our Sun, we are talking about 15 million kelvins. For the stars with the lowest range of temperature, such as the Sun, the main process is proton-proton fusion (figure 1.3) which happens to be highly slow. It can take up to hundreds of millions of years for a proton to fuse with another one. As one can already imagine, considering such a slow process on the Earth to produce energy is illogical. The other mentioned ways are understandably less viable since they need even higher temperatures and more extended timings. What can be done then?

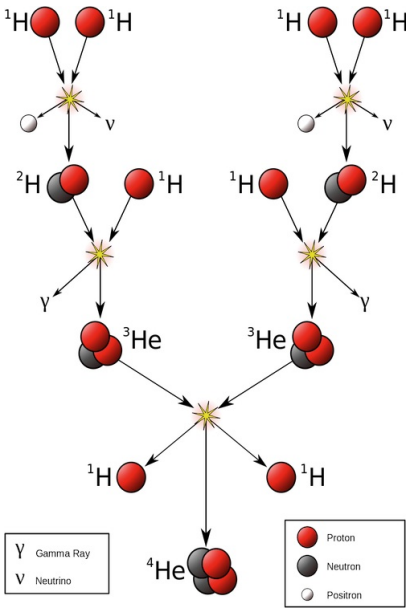

Figure 1.3: Proton-proton fusion process. Source: [10]

At the beginning of the 50s, the first experiments on nuclear fusion commenced having promising results by using two elements: deuterium and tritium. Deuterium is obtained from seawater, while tritium is easily acquired by adding a neutron to the nucleus of a lithium atom, which from we posses great amounts. There are two possible reactions for the obtaining of tritium from lithium:

$$Li^6 + n \rightarrow T + He^4 + 4.8MeV \tag{1.1}$$

$$Li^7 + n \rightarrow T + He^4 + n - 2.5MeV \tag{1.2}$$

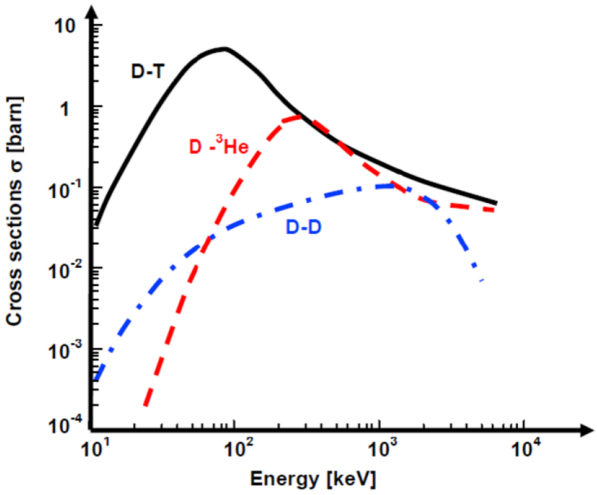

Figure 1.4: Effective cross section for different nuclear fusion reaction. Source: [11]

Deuterium, lithium and so tritium as well, are promising nuclei because of their abundance on Earth. Also, and it is something that concerns a big part of the population when discussing nuclear physics, both nuclei are not radioactively harming. Deuterium is, in fact, not radioactive at all. Meanwhile, Tritium is a radioactive isotope that decades into beta decay emitting quite low energy electrons which are not considered harmful for DNA. Only in massive amounts and long and constant exposure, which is completely not the case we contemplate, Tritium seems to have effects on DNA and not in a mortal way [12]. For these reasons, nuclear fusion is meant to be a green and free of radioactive residues energy source. In addition, as one can see in figure 1.4, the D-T reaction in comparison to other reactions, possesses a significantly large effective cross-section for relatively low energies based on the range of great energies we are working with.

The most common fusion reaction is given between the deuterium and the tritium nuclei resulting into a helium one as it follows:

$$ {}^{2}_{1}D + {}^{3}_{1}T \rightarrow {}^{4}_{2}He + {}^{1}_{0}n + 17.6MeV \tag{1.3} $$

An energy of 17.6 MeV is obtained per reaction. To have an overview of how energetically dense nuclear fusion is, let's introduce some significant numbers: just 1kg of the fuel particles used in the reaction above (1.3), would liberate an energy of 10^8 kWh [13]. This means 1GW of electrical power a day. It is symbolically described as if one glass of water could provide enough energy to a family of four for an average life of 80 years. A dream that might come true in the next decades.

Quantum tunneling can help making the reaction (1.3) happen, but that alone is not enough. It is needed to induce sufficient energy so that both the nuclei D and T get close enough for them to fuse. The best method to do that is by heating both nuclei to very elevated temperatures in order to increase their thermal velocities sufficiently. This concept is the so called thermonuclear fusion.

When referring to high temperatures, one must think of around 100 million of degrees centigrade. Such a temperature is equivalent to 10 keV. It is relevant to note that in fusion physics, to express temperature, energy units are used. This magnitude is equivalent to the kinetic energy of each particle composing the plasma. It is also important to note that $\frac{1MeV}{K_B} = 11604.51812K$, where k_B is Boltzman's constant. Under such elevated temperatures, matter becomes completely ionized, meaning that electrons are ripped away. As a result we have an ionized gas known as plasma. This one is one of the main characters in nuclear fusion .

1.2 Plasma

Plasma is known as the fourth state of matter after solid, liquid and gas. As defined in the previous chapter, when heating matter to super high temperatures, the electrons are removed from the atoms leading to an ionized gas. Over 99% of the universe is considered to be plasma. A great amount of such a percentage are stars.

Inside this state of matter, moving particles can create local concentrations that are

able to interact with others due to Coulomb force. Thus, a more collective behaviour of plasma must be taken into account. The movement of particles does not only depend on local conditions but on collective ones as well.

Since plasma happens to be a quite good conductor, the electric field in it, is so low it can be considered almost null. For that reason plasma is a quasineutral state, being its number of negative particles (n_e) nearly equal to the number of positive particles (n_i). This is: $n_e \approx n_i$

Plasma is being object of many studies and applications, such as rocket propulsion, computer chips or healing wounds, to name a few. But as it has been already introduced, it also plays a great role in the search for fusion energy and controlling plasma is one of the main goals. A new question must come now to our minds: where and how is it possible to confine plasma under such extreme temperatures? Introducing "tokamaks".

1.3 Tokamaks and plasma confinement

There are a three main ways and methods to make plasma confinement possible: gravitational, inertial and magnetic. The first one is the most successful one, as it is seen in stars, but it is impossible to reproduce on Earth. The inertial method, on its part, uses quite powerful lasers to compress the fuel in a pretty compact space relying on the pressure done by radiation. As a consequence of the compactness, nuclear fusion takes place. Nonetheless, magnetic confinement seems to be the most promising one, and it will be developed in the following paragraphs.

In order to magnetically confine and control plasma, at the beginning of the 50s in the Soviet Union, a new device was devised: the tokamak. Since then, decades of advances and investigation have been dedicated to improve the first tokamaks to the ones we now have. Although, it is still a developing field.

A tokamak is a plasma confinement system with a toroidal shape in which a strong magnetic field accelerates the particles into a helical movement and keeps the hot plasma from being in contact with the inner walls of the tokamak. In figure 1.5 one can see a

representation of a conventional tokamak seen from outside and inside. This concept is named magnetic confinement. To understand the principles of this system, some basic magnetism ideas shall be first introduced.

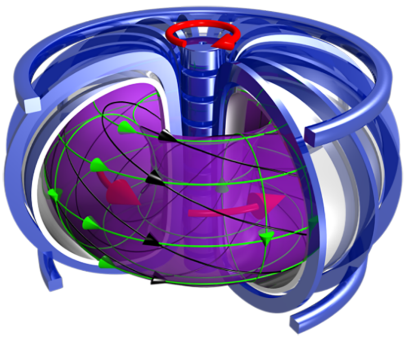

Figure 1.5: Conventional Tokamak. Source: [14]

Considering a non existing electric field, as a charged particle with charge q, just like the ones in plasma, moves with a velocity $\vec{V}$ in a magnetic field $\vec{B}$, a force will be experienced by such a particle. This force is known as Lorentz Force (1.4).

$$\vec{F} = q(\vec{V} x \vec{B}) \tag{1.4}$$

For a velocity $\vec{V}$ with perpendicular and parallel components to the magnetic field, it is necessary to distinguish two cases. Regarding the parallel component to the magnetic field, it is easily seen that $\vec{V}_{||} \mathrm{x} \vec{B}$=0 due to vector product properties. Thus, $\vec{F}_{||}$=0. And so recalling Newton's laws:

$$\vec{F}_{||} = m\frac{\mathrm{d}\vec{V}}{\mathrm{d}t} = 0 \longleftrightarrow \vec{r} = \vec{r}_0 + \vec{V}t \tag{1.5}$$

Consequently, the particle describes a rectilinear movement. On the other hand, when taking into account the perpendicular direction to the magnetic field, a more interesting situation must be studied. Since $\vec{V}_{\perp}$ and $\vec{B}$ have now different directions, $\vec{V}_{\perp} \mathrm{x} \vec{B} \neq 0$. Hence:

$$\vec{F}_{\perp} = q(\vec{V}_{\perp} x \vec{B}) = m\vec{a} \tag{1.6}$$

Where from now on, V will only make reference to the perpendicular component of the velocity. Therefore, $\vec{a}$ is easily obtained as it follows:

$$\vec{a} = \frac{q}{m}(\vec{V} x \vec{B}) \tag{1.7}$$

The acceleration has as well two components, tangential and normal one, $\vec{a}_t$ and $\vec{a}_n$ respectively. The acceleration in its tangent component turns out to be null. Consequently, the particle is describing a circular trajectory. And since

$$a_n = \frac{V^2}{r} \tag{1.8}$$

then,

$$a_n = \frac{V^2}{R} = \frac{q}{m} V B \tag{1.9}$$

From which both expressions for the so-called ciclotron frequency (1.10) and Lamor's Radius (1.11) can be obtained:

$$\omega_c = \frac{qB}{m} \tag{1.10}$$

$$R = \frac{Vm}{qB} \tag{1.11}$$

Both rectilinear and circular movements together result in the helical trajectory already mentioned at the beginning of this chapter.

In other matters and continuing with magnetism, it is fundamental to know there is not only one magnetic field in a tokamak but two, since the toroidal field, $\vec{B}_{tor}$, can not confine plasma just by itself. With regards to the toroidal field in question, a difficulty is found. Such a field is not constant. Indeed, it depends on the distance between the toroid center and the particles from the plasma. As a consequence, there is a magnetic field gradient, $\nabla \vec{B}_{shift}$, which makes positive ions move upwards and electrons go downwards. Therefore, an electric field appears, creating another shift, $\vec{E} x \vec{B}_{shift}$, that pushes particles in the direction of the walls from the toroid. To solve this, a poloidal magnetic field $\vec{B}_{pol}$ is as well required. This one is caused by current flowing in the toroidal direction inside the plasma, which according to the right-hand rule, creates a magnetic field with circular shaped lines in its perpendicular plane and so, such wished polodial magnetic field.

It is the combination of $\vec{B}_{tor}$ and $\vec{B}_{pol}$, which we referred to when explaining helical trajectory caused by a magnetic field inside the tokamak. Owing to this kind of movement, field lines are parallel and close enough for the particles to collide and fuse. Besides, it keeps the particles confined in the central region to prevent the hot plasma from cooling and interacting with the inner walls of the tokamak. In other words, it is the principle for nuclear fusion to be possible inside a tokamak. In figure 1.6 one can see graphically the directions of $\vec{B}_{tor}$ and $\vec{B}_{pol}$ respectively.

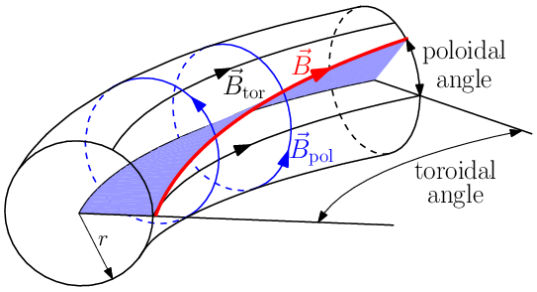

Figure 1.6: Toroidal and poloidal magnetic field. Source: [15]

A tokamak has then both toroidal field coils that produce the toroidal field and solenoids that induces the current in the plasma in order to generate the poloidal magnetic field. In addition, poloidal field coils are set to shape the plasma in the required geometry.

In order to measure a reactor's efficiency, a new parameter shall be introduced, Q. Where:

$$Q = \frac{\text{Power acquired by the reactor}}{\text{Power supplied to the reactor}} \tag{1.12}$$

For a $Q > 1$, energy is obtained. This have not been the case yet. The closest value has been so far of $Q = 0.62$, achieved in the JET tokamak, UK [16]. Meanwhile, $Q > 1$ will not be possible until Lawson criteria is satisfied [17]. That is, the following expression must be fulfilled:

$$nT\tau > 5x10^{21} keV\, sm^{-3} \tag{1.13}$$

Where n is ions density, T is the temperature of plasma and τ the confinement time respectively.

Currently, there are roughly 50 tokamaks worldwide distributed. All of them have their own characteristics and sizes and are part of different researches. Recently at University of Sevilla, a new device is being constructed: The SMART tokamak.

1.4 The SMART tokamak

The name SMART [18] refers to SMall Aspect Ratio Tokamak, where aspect ratio is defined as the major radius over the minor one ($\frac{R}{a}$). One can have a more graphical

explanation in the following figure 1.7:

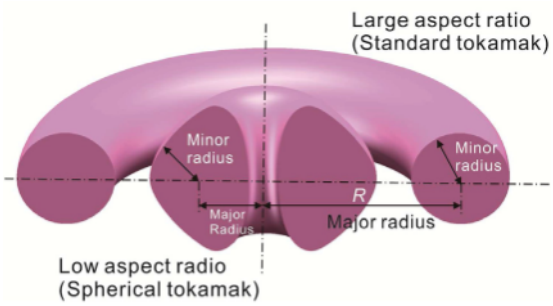

Figure 1.7: Comparison between small (low) aspect and large aspect ratio tokamak. Minor and major radius are shown. Source: [19]

As tokamak designs evolved, it was found out that by changing its original "Doughnut" shape to an spherical one, which means an aspect ratio <2, it does not only make such a construction more compact, but also more efficient with a higher plasma pressure.

The SMART tokamak (figure 1.8), is a spherical tokamak with a plasma major radius of $R \simeq 0.50m$ and minor radius $a \simeq 0.25m$. It will operate under plasma currents of $0.5\,MA$ and magnetic fields up to 1T. It has 12 toroidal and 8 poloidal coils, plus one solenoid. Since for the moment, SMART will be part of study for a future energy generation based on nuclear fusion, every "practice" and experiment made with it, will not be working on D-T fusion reaction to avoid wasting Lithium. Instead, for triangularity and diagnosis studies, Hydrogen will be mostly used. In the following sections, H-mode and triangularity will be introduced.

Figure 1.8: The SMART Tokamak, located in Seville, Spain. Source: Plasma Science and Fusion Technology Group, Private Communication

1.4.1 H-Mode

The "H" from H-mode refers to High confinement regime during neutral beam heating experiments on tokamaks. This means a more elevated confinement time. That is to say, heat takes longer to escape from plasma.

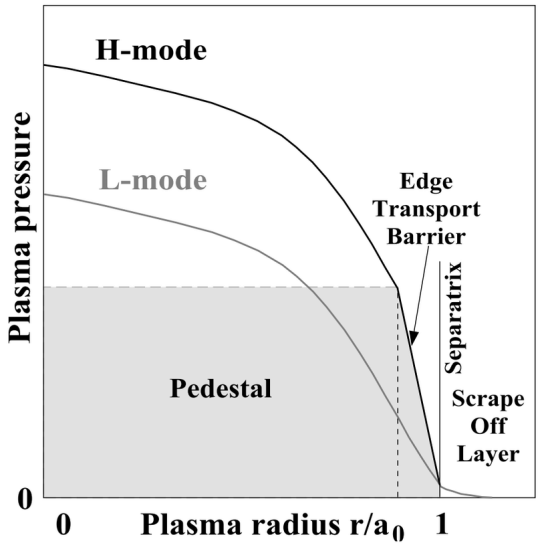

Figure 1.9: Plasma profile in L-Mode and H-Mode regimes. Source:[20]

In 1982, while studying plasma in ASDEX (Axially Symmetric Divertor Experiment), Friedrich Wagner and his researching group found that under certain energy conditions there is a sudden transition to a higher confinement [21]. This occurs firstly at the edge of the plasma since it is where a rapid increase of density takes place and thus an increase in the gradient of pressure. This effect appears due to the formation of the so-called edge transport barrier (ETB), which reduces the level of transportation at the plasma edge. It is a highly important concept in plasma confinement. The gradient of pressure is as well the responsible for the appearance of a characteristic pedestal structure, as seen in figure 1.9.

For the transition to H-mode to be possible, external heating is required, which can be made with neutral beam injection (NBI). When the injected particles collide with plasma, they become ionized and as a result confined, donating all their energy to the plasma. In addition, a radial electric field also appears at the edge of the plasma [22]. Indeed, the gradient of such a field is considered to be the possible reason for the pressure gradient and so the transition to H-mode. Nonetheless, it is not completely clear yet.

However, when it comes to H-mode, an inconvenience appears. It is this gradient of pressure at the edge of plasma the responsible for the so-called Edge Localized Modes

(ELMs). These suppose magnetohydrodynamic perturbations which lead to high thermal charges at the wall of the reactor. This is clearly an effect that shall be avoided, since magnetohydrodynamic perturbations would rapidly prevent plasma confinement from succeeding. They do in fact, quickly decrease pressure and current. For this reason, the SMART tokamak will make use of negative triangularity plasma, which seems to be a promising solution. It does work with a very similar confinement level to H-mode with the advantage of not presenting any of the ELMs perturbations.

1.4.2 Plasma Shape. Triangularity

When studying nuclear fusion, the shape of the plasma inside a tokamak plays a great role since it can determinate the difficulty in the plasma confinement making. The most convenient shape is one like the letter "D" in its capital form.

On its part, triangularity is merely the horizontal distance between the plasma's maximum radius and the so-called X-Points, where the polodial field has a null magnitude. Then, one can distinguish between positive and negative triangularity. The first one consists in the straight part of the D shape opposite to the toroid's hole from the tokamak. On the contrary, when it is the curve part from the D shaped plasma facing the toroid's hole, we talk about negative triangularity. A graphical description is given in figure 1.10.

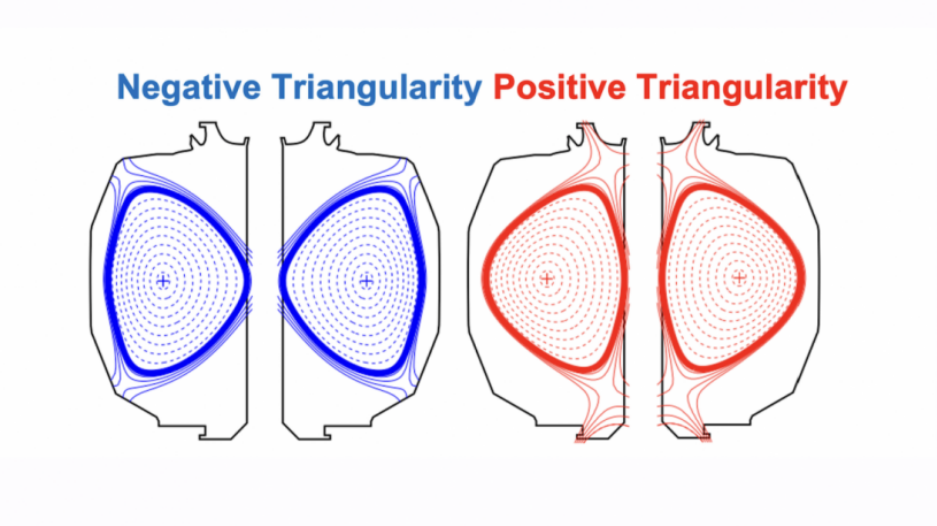

Figure 1.10: Positive and negative triangularity of plasma. Source: [23]

Recently, it has been found that negative triangularity reduces the interaction between the plasma and the facing materials at the inner walls of the tokamak, which so far was an obstacle in nuclear fusion production. This prevents the walls from the tokamak from rapid damage due to the high temperatures from plasma. Thus, negative triangularity is a potential shape for plasma in future tokamak devices.

1.5 Objectives

Charge exchange recombination spectroscopy is a powerful diagnosis method that provides information about different parameters of plasma. It involves a reaction between a donor ion and a receiver ion. Such technique will be explained in more detail in the following chapters.

Part of the interest of this study relies on obtaining the required effective emission rates for different receiver elements making use of the data taken from OpenADAS [24]. A database from which the information of the bombarding energies and the CXRS cross sections will be downloaded for different n and l, being those the quantum numbers. The most convenient charge exchange reaction for SMART tokamak will be, as well, identified. Thus, the working methods and the acquired results from this study will be presented and discussed in the following chapters. But first, charge exchange recombination spectroscopy will be introduced.

2 Charge exchange recombination spectroscopy

Once established the main concepts that should enable the reader to understand the principles of plasma and tokamaks, the theory behind Charge Exchange Recombination Spectroscopy, also known as CXRS, will be explained. But before delving into the subject, it is worth noting the importance of plasma diagnostics. They have been developed to study certain topics and characteristics of plasma in the path of tokamaks research. There are different diagnostics, each of them with its own purpose, but they all are key in the search for fusion energy based on plasma confinement.

Charge exchange recombination spectroscopy is used for plasma diagnosis, providing information about the impurity ions temperature, rotation and density along the lines of sight (LOS). The method for CXRS consists in the injection of neutral particles in the plasma. After an electron transference, the impurity ion is now in an excited state and so it decays to a lower energy state emitting a characteristic radiation. Such energy will be afterward measured in the form of spectroscopy. This process takes place according to the following reaction:

$$H + A^{Z+} \rightarrow H^{+} + A^{(z-1)+*} \rightarrow H^{+} + A^{(z-1)} + h\nu \tag{2.1}$$

Where H is a neutral atom of hydrogen or deuterium, A is an ion of Z charge and $h\nu$ is the energy of the emitted photon.

Lines of sight refer to the geometrical path throughout measurements are taken when the measurements are being done. They represent the directions that each channel of the CXRS diagnostic instrument illuminates. In the following figure (2.1) one can see in

green colour the LOS in region from ASDEX Upgrade.

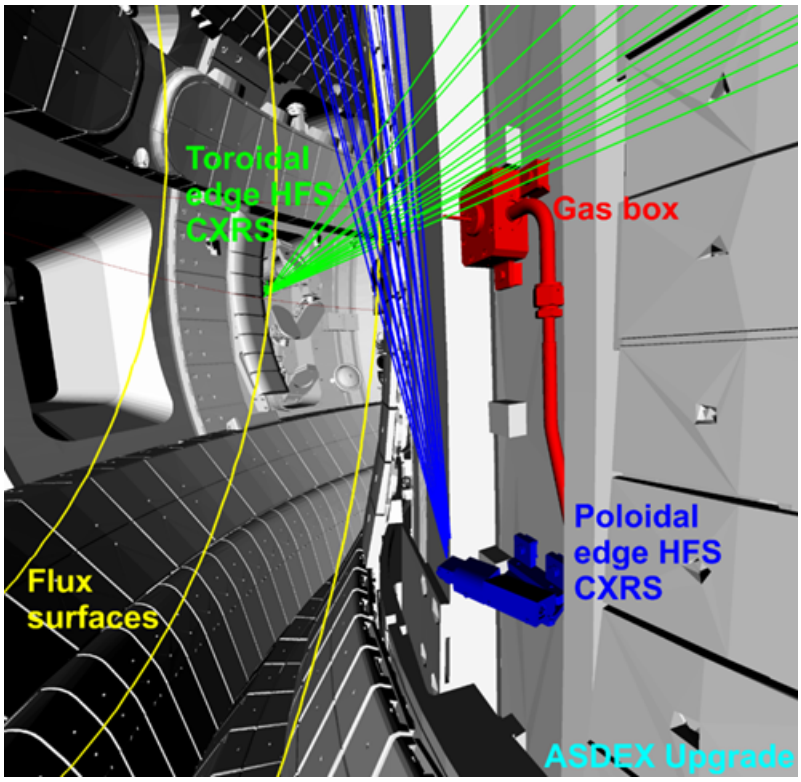

Figure 2.1: CXRS LOS in Asdex Upgrade. Source: [25]

CXRS can be either done with neutral beam injection (NBI), which is done by injecting high energy neutrals, or as it is the case in the SMART tokamak, with neutral gas puff (GP). This last one is made by injecting a thermal neutral gas in the plasma. When thermal molecular deuterium is injected inside the plasma, due to Frank-Condon effect, one particle of deuterium divides into two neutral atoms of deuterium, each with an energy of around $3eV$. Nonetheless, from both particles only one will make it to interact with the plasma. The other one, normally, returns back towards the wall. It is the particle that gets into the plasma, the one that will initiate the reaction above (2.1) and make charge exchange recombination spectroscopy possible.

It is worth to mention that the GP method has advantages over NBI. Contrary to this one, the necessary devices such as the gas delivery tube, can be located in almost any part of the plasma. Over more, it is cheaper, less complex and easier to execute than NBI. Nevertheless, GP has as well some drawbacks which must not be ignored. For instance, as the core of the plasma is reached, a rapid decay of signal is seen, since slow neutral

particles experiment a decrease in the penetration power. Thus, GP-CXRS can only be successfully used at the edge of plasma. And yet, this does not suppose a major problem when studying the pedestal region as the edge covers the region one wishes to analyse with CXRS.

As explained before, CXRS is used in order to obtain information about ion impurities temperature, rotation and density. The emitted light from charge exchange is recollected by optical fibers and analysed by using an spectrometer. One has an spectra for each LOS of the CXRS diagnosis. Fitting these spectra, a radial profile of temperature and rotation can be determined by making use of Doppler broadening [26] and shift on the acquired spectral lines. Nevertheless, for ion impurities density the path is not that simple.

2.1 Impurity ion density evaluation

In order to measure impurity ion density, more information than just the spectral lines is needed. The procedure for obtaining such parameter will be developed in this section. But first, one must get to know what we refer to when talking about impurities. In a plasma, impurities are defined as particles that do normally not benefit the process of fusion. However, they might have negative or positives effects in the reaction of fusion and plasma confinement. It is then, necessary to understand how they work and to study the density of impurities that are found in plasma under certain conditions. These impurities can be present from the wall of the reactor or might be injected on purpose in the plasma. In future reactors, there will also be alpha particles as impurities that will come from the fusion reactions [13].

To obtain the desired impurity ion density, one must first take a look into the measured intensity $Lcx, z(\lambda)$. Before introducing its mathematical expression, it shall be already anticipated, that for gas puff based CXRS, it does not only depend on ion impurity density but also on the density of two neutral populations. Here is where the obstacle in impurity density evaluation lies. The first neutral population corresponds to the injected neutrals. The second one, on its part, is known as the halo neutral, a cloud of thermal neutral particles that appears due to CXRS between the injected neutrals and

the main ions in plasma if considering that both species coincide. The halo neutral is able to undergo CXRS with impurity ions resulting on extra emission rates. Both populations must be studied and analyzed independently since they all contribute on different ways to the total CXRS emission. The expression for the measured CXRS intensity will be now described as it follows:

$$L_{CX,Z}(\lambda) = \frac{h\nu}{4\pi} \sum_{n} \sum_{j} \int_{LOS} n_Z(s) n_{o,n,j}(s) \langle \sigma_{(n,j,Z,\lambda)} v_j \rangle_{eff}(s) ds \tag{2.2}$$

Where n_z is the impurity density one wishes to determine. Although (2.2) can be solved for n_z, it is necessary to understand first every term and the expression above. To start with, λ describes the specific emission rate being evaluated and $h\nu$ corresponds to the energy of the photon. The sums on n and j are over both quantum numbers. Inside the integral along the LOS, we do not have only n_z but also another density, $n_{o,n,j}(s)$ the neutral density populations mentioned before. Furthermore, $\langle \sigma v \rangle_{eff}$, is the effective CX emission rates. σ corresponds to charge exchange cross-section while v to the collision velocity. "$\langle\rangle$" refers to an average since every specie has a certain velocity distribution. $\langle \sigma v \rangle_{eff}$ will be playing a great role in the next chapters. Finally, s refers to the coordinate along the LOS. Considering the case in which n_z is constant along the LOS, solving for n_z, the following expression is obtained:

$$n_z = \frac{4\pi}{h\nu} \frac{L_{CX,Z}(\lambda)}{\sum_n \sum_j \int_{LOS} n_Z(s) n_{o,n,j}(s) x \langle \sigma_{(n,j,Z,\lambda)} v_j \rangle_{eff}(s) ds} \tag{2.3}$$

3 Emission rates calculation for GP-CXRS

In this chapter the followed working route and method will be introduced as well as the obtained results. Every step in calculus will be explained in detail through the different sections.

3.1 Working method

As charge exchange cross-sections must be obtained, the calculation will begin with the raw cross sections and transform them into emission rates by making use of the expressions presented in the next section. Different corrections must be applied, such as nl-cascade and l-mixing rates.

The first objective is to achieve similar figures for CX cross-sections versus temperature to the ones obtained by "R.M Mcdermott et al." at [1]. Being able to reproduce the same figures gives us the confidence to confirm that our code and procedure is correct. The idea is therefore, to write a code on Pyhton that allows us to transform the data into emission rates and apply every needed correction in order to obtain such mentioned graphics. Once the code works as wished, any reaction can be introduced with the certainty of getting correct results. This way, one is able to study different possible candidates as receiver ions in CXRS reactions and analyse which would be the most promising one for charge exchange diagnosis at SMART.

One can see the results from [1] in figure 3.1. Charge exchange reactions are studied

for deuterium as the donor ion and the receiver ions shown in table 3.1, together with the references for the data used. Only for Nitrogen, the data is taken from a different source than OpenADAS. $n = 1$ and $n = 2$ refers to the states of the donor particle, being $n = 1$ de ground state and $n = 2$ the first excited state .

In addition, as explained in section 2.1, when obtained $\langle \sigma v \rangle_{eff}$, ion impurity density can be determined. Hence, the values for $\langle \sigma v \rangle_{eff}$ are required. Effective emission rates can be calculated for any receiver element. A general method to determine the equation for $\langle \sigma v \rangle_{eff}$ will be now introduced, which indeed will be solved for the concreted data in table 3.1.

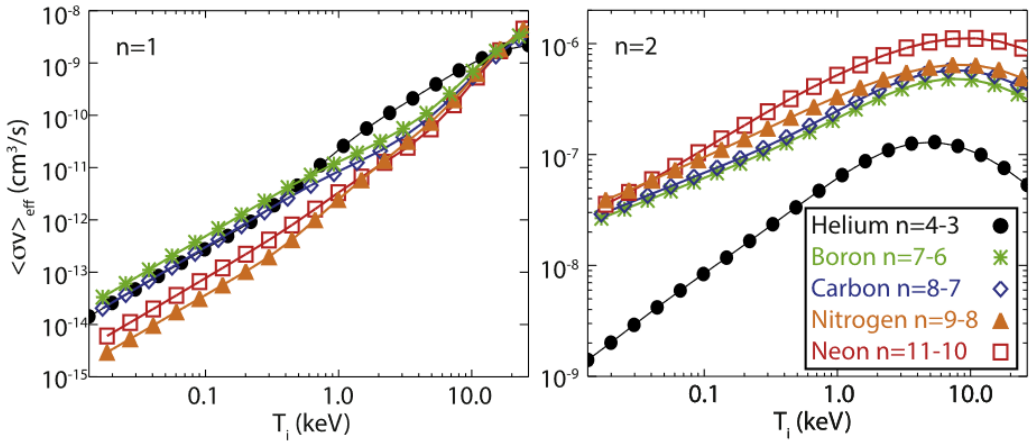

Figure 3.1: Effective emission rates in cm^3/s versus temperature in keV from "Evaluation of impurity densities from charge exchange recombination spectroscopy measurements at ASDEX Upgrade". Source: [1]

ELEMENT	$n = 1$	$n = 2$
He: $n = 4 - 3$	qcx#h0_old#he2.dat	qcx#h0_en2_kvi#he2.dat
C: $n = 7 - 6$	qcx#h0_old#c6.dat	qcx#h0_en2_kvi#c6.dat
Ne: $n = 11 - 10$	qcx#h0_old#ne10.dat	qcx#h0_en2_kvi#ne10.dat
B: $n = 7 - 6$	qcx#h0_old#b5.dat	qcx#h0_en2_kvi#b5.dat
N: $n = 9 - 8$	From Igenbergs	From Igenbergs

Table 3.1: Data used for CXRS reactions from OpenADAS adf01 files [24] and Igenbergs [27] for Nitrogen for $n = 1$ and $n = 2$

3.2 Effective emission rates calculation

Considering the approximation of plasma as a fluid that obeys a quasi-equilibrium state, the distribution function that describes it the best is a Maxwellian distribution [13]. Such is expressed as it follows:

$$f_j(v_j) = n_j \left(\frac{m_j}{2\pi T} \right)^{3/2} \exp\left(-\frac{m_j v_j^2}{2T} \right) \tag{3.1}$$

Being n_j the density and m_j the mass of each particle. Every particle has as well a velocity v_j. And finally, T is the temperature.

Given the CXRS reaction, for the donor particle being called by a "d" and the receiver by an "r", taking into account both particles, the total reaction rate per unit volume results in:

$$\boldsymbol{R} = \int \int \sigma(v') v' f_d(v_d) f_r(v_r) d^3 v_d d^3 v_r \tag{3.2}$$

Where σ is the cross section and v' is the difference between velocity of the donor and the receiver, $v' = v_d - v_r$. Thus, $\boldsymbol{R}$ can be written in the next form:

$$\boldsymbol{R} = n_d n_r \frac{(m_d m_r)^{3/2}}{(2\pi T)^3} \int \int \exp\left(-\frac{m_d + m_r}{2T} \left(V + \frac{1}{2} \frac{m_d - m_r}{m_d + m_r} v' \right)^2 \right) \sigma(v') v' exp\left(-\frac{\mu v'}{2T} \right)^2 d^3 v' d^3 V \tag{3.3}$$

For m_d the mass of the donor ion and m_r the mass of the receiver ion.

Being

$$\mu = \frac{m_d m_r}{m_d + m_r} \tag{3.4}$$

and

$$V = \frac{v_d + v_r}{2} \tag{3.5}$$

As that the integral over V is $(2\pi T/(m_d + m_r))^{3/2}$, and taking into account that the energy of the bombarding particle, which is normally given in experiments, has the expression of the kinetic energy

$$\epsilon = \frac{1}{2} m_d v'^2 \tag{3.6}$$

Besides that the final effective emission rate is determined by dividing $\boldsymbol{R}$ by both donor and receiving ion densities:

$$\langle \sigma_{(n,j,Z,\lambda)} v_j \rangle_{eff} = \frac{\boldsymbol{R}}{n_d n_r} \tag{3.7}$$

We can arrive to a final expression for $\langle \sigma_{(n,j,Z,\lambda)} v_j \rangle_{eff}$

$$\langle \sigma_{(n,j,Z,\lambda)} v_j \rangle_{eff} = \left(\frac{8}{\pi}\right)^{1/2} \left(\frac{\mu}{T}\right)^{3/2} \frac{1}{m_d^2} \int \sigma(\epsilon) \epsilon \exp\left(-\frac{\mu\epsilon}{m_d T}\right) d\epsilon \tag{3.8}$$

3.2.1 Charge exchange cross sections

Every cross section data for each of the studied transitions has been extracted, as mentioned before, from OpenAdas [24]. Arrays for energy values in keV and the raw CXRS cross-sections in cm^3/s are obtained. When plotting the resulting data, the following figures (Figure 3.2) for $n = 1$ and $n = 2$ can be studied:

In figure 3.2, one can appreciate the proportional dependence of the CXRS cross-section on the collision energy for low energy values. For nitrogen, the data used includes larger collision energies, thus, one can see how the cross section decreases for the highest values of energy. Furthermore, an increase of two orders of magnitude can be noted for $n = 2$ in comparison with $n = 1$. Hence, even a very small population of excited neutrals must be considered in impurity densities calculations [28]. Effective emission rates must be now calculated.

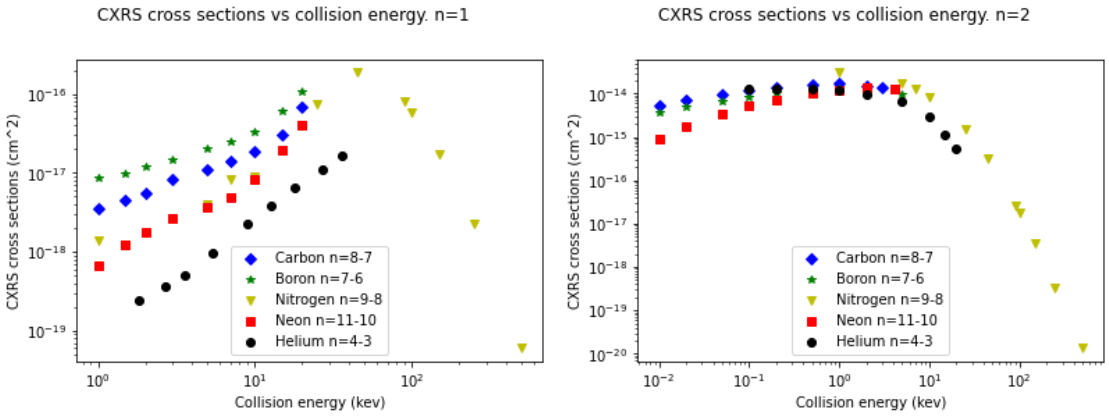

Figure 3.2: CXRS cross section versus collision energy for $n = 1$ and $n = 2$, respectively for data in table 3.1 in logarithmic scale.

3.2.2 Thermal charge exchange effective emission rates

Recalling the expression 3.7 and applying it to the CXRS cross-sections presented above, a new code is now written that treats the raw cross sections in order to transform them into the wished effective emission rates. However, no nl-cascade and l-mixing effect corrections are yet applied. These will be introduced in the next chapters. It is interesting to study how corrections affect the results. For this reason, the results obtained by exclusively applying the Maxwellian average developed in section 3.2 will be first presented. In figure 3.3 the resulting CXRS cross sections against temperature in keV for the states $n = 1, n = 2$ are shown.

As one can see, by comparing figure 3.1 with 3.3, a noticeable difference arises in the results for the effective emission rates. For $n = 1$, a more linear representation should be obtained, and yet, for temperatures below 0.2 keV and over 3 keV, figure 3.3 shows slightly curved results as well as differences in the maximum and minimum values for y-axis. For $n = 2$ as well, maximum values of effective emission rates for every receiver element are shifted almost 10 kev in the temperature axis and they also differ from the minimum and maximum values of effective emission rates themselves. Even a larger difference appears in results for the case of Nitrogen. This is due to two effects already mentioned before, that shall not be ignored: n-l cascade and l-mixing effect.

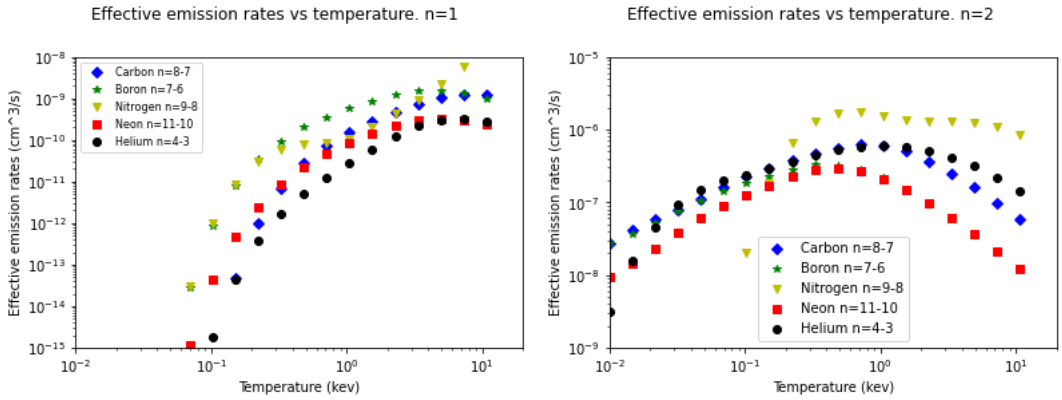

Figure 3.3: Effective emission rates in cm^3/s for the date in table 3.1 versus temperature in keV for $n = 1$ and $n = 2$ respectively. No nl-cascade and l-mixing effect corrections applied.

3.2.3 n-l cascade correction

In charge exchange reaction, the electron from the neutral source particle will tend to transfer to excited levels. As a consequence, the effective cross section depending on the quantum numbers n and l, $\sigma(n) = \sum_l \sigma(n,l)$, reaches a maximum in n, where $n_{max} \approx Z^{3/4}$. In addition, there is a direct relation between the collision energy and the width of the distribution in n. The higher the collision energy, the bigger such distribution gets and so more n states are populated. As for every n number there is $l = 0, ..., n-1$, l increases as n does so. Thus, the l distribution for $\sigma(n,l)$ for a given n state is as well peaked. As one can imagine, the $\sigma(n,l)$ increases with l. Furthermore, those transitions between states near or below n_{max}, states with high l, will be more populated and transitions where $\Delta n = 1$ are the most intense ones. Hence, every $\sigma(n,l)$ for each l number for a given n must be taken into account [29].

A new concept is then introduced, n-l cascade. In CXRS, the cascade of the excited electrons from the initial distribution determine the final observed intensities. Consequently, a resulting $\sigma(n,l)$ is obtained presenting a slight difference in value in comparison to the initial theoretical $\sigma(n,l)$. For a transition given by $n \to n'$, the total effective cross-section is determined by summing over every l level for a given n state. The following expression (3.8) describes the wished total effective cross section with nl-cascade

correction applied:

$$\sigma(n, n') = \sum_{l=0}^{n'-1} \sigma(n', l) b_{nl,n'l'} \tag{3.9}$$

Where $b_{nl,n'l'}$ are the branching ratios for each level. For our calculations, data for branching ratios from [30] will be used.

It has been observed that for transitions between lowest n states, the total effective cross-sections, $\sigma(n, n')$ differs the least from the original ones $\sigma(n, l)$ [29]. Therefore, applying (3.8) to the raw cross-sections taken from OpenAdas, total effective cross-section are obtained. These ones will be again transformed by making use of Maxwelliam distribution (3.7). In the figure below (3.4), the resulting rates with nl-cascade corrections are represented for every used receiver element against temperature.

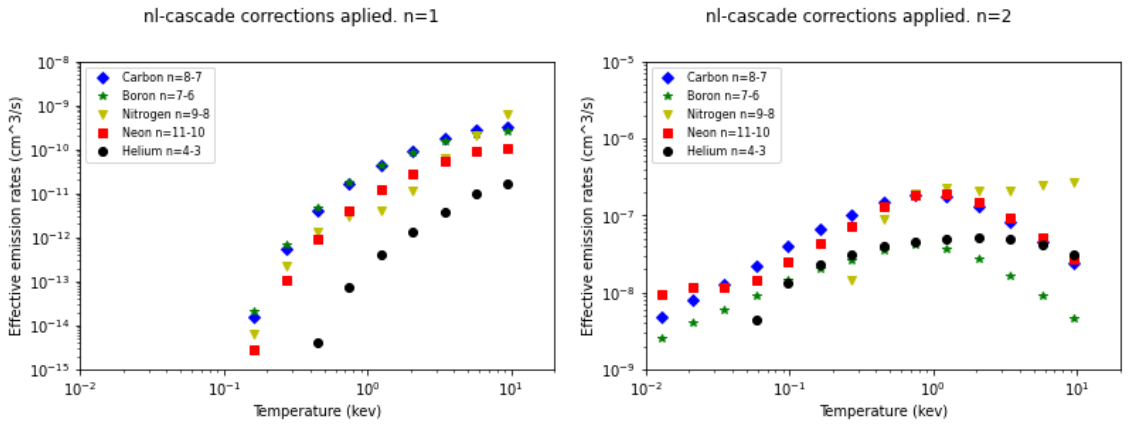

Figure 3.4: Effective emission rates in cm^3/s for data in table 3.1 for $n = 1$ and $n = 2$ respectively with nl-cascade correction applied.

In order to show the striking difference between the results where no correction has been applied and nl-cascade corrected ones, the following plot is shown (figure 3.5) overlapping the effective emission rates for CVI in both analysis.

As seen in figure 3.5, both effective emission rates for $n = 1$ and $n = 2$, suffer an decrease for the case of nl-cascade correction applied in comparison to the first results calculated in section 3.2.2. For the lowest values of temperature, a more considerable difference between effective emission rates appears for the same state n. Nevertheless, these are not the wished results yet. l-mixing effect must be taken into account.

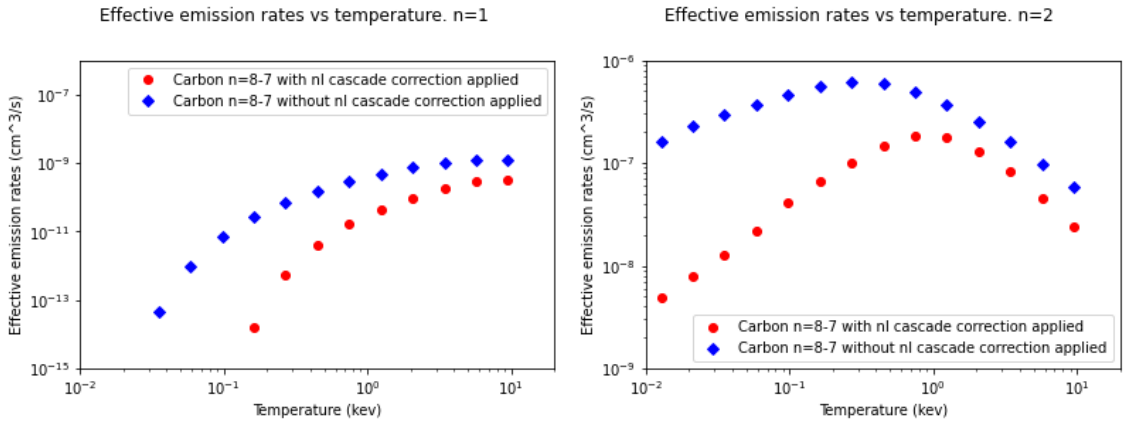

Figure 3.5: Effective emission rates in cm^3/s for CVI versus temperature in keV for $n = 1$ and $n = 2$ respectively, overlapping no correction applied and nl-cascade correction applied.

3.2.4 l-mixing effect correction

The surrounding plasma environment can, to a large extent, affect the cascade process. In fact, a transfer between different l levels can occur before an electron drops to lower states via photon radiation. This effect is known as l-mixing process and it can significantly affect the original CX cross-sections. l-mixing is able to change the populations in the excited levels as well as to affect line intensities and fine-structure line profiles [29].

l-mixing rates typically refer to the rates at which different rotational levels of an atom or molecule mix due to collisional processes. Each rotational energy level of an atom (or molecule) can be perturbed or mixed by colliding with other particles. Such rotational energy is characterized by the angular momentum, $\boldsymbol{J}$. Where:

$$J = L \oplus S \tag{3.10}$$

Being S the total spin and L the total orbital angular momentum for a system of particles. Where $L = l_1 \oplus l_2$, with l_i, the quantum number for $i = 0, 1, ..n - 1$. This means that, for a state n there are $l = 0, ..., n - 1$, and so every l must be considered.

Thus, for CX reactions, the l-mixing effect due to ion-ion collision must be taken into account. For this thesis, the model developed and studied by Pengelly and Seaton [31] has

been perused. There are, as a matter of fact, more and newer publications on this topic that are more precise for the case we treat. Pengelly and Seaton considered their model for planetary nebulae where the Coulomb repulsion between ions is ignored. However, it is one of the most used methods to determine l-mixing rates. R.J Fonck et al. in the paper "Determination of plasma-ion velocity distribution via charge-exchange recombination spectroscopy", [29] adapt the mentioned model to the case of plasma and the conditions that are found in it. Indeed, it is the model applied by the followed reference [1] as it is the method used by the ADAS codes. The math is explained as it follows:

For a $n, l \rightarrow n', l'$ transition, where $l' = l \pm 1$, the l-mixing rate coefficient between levels in hydrogenic ions, with charge Z, colliding with ions of charge z, is given by:

$$q_{nl}^{Z,z} = 9.93x10^{-6} \left(\frac{\mu}{m}\right)^{1/2} \frac{D_{nl}}{T_i^{1/2}} \left(11.54 + log_{10}\left(\frac{T_i m}{D_{nl}\mu}\right) + 2log_{10}\overline{R}_c\right) \tag{3.11}$$

where

$$D_{nl} = \left(\frac{z}{Z}\right)^2 6n^2(n^3 - l^2 - l - 1) \tag{3.12}$$

and

$$2log_{10}\overline{R} \approx 1.68 + log_{10}\left(\frac{T_i}{N_e}\right) \tag{3.13}$$

With μ the reduced mass for both colliding ions and T_i the ion temperature in Kelvin. m is the electron mass and N_e the electron density. $q_{nl}^{Z,z}$ has units of cm^3/s while N_e of cm^{-3}. For several ion species, as it is the case we study, the total l-mixing rate for a $n, l \rightarrow n', l'$ transition, is then given by:

$$\sum_z N_z q_{nl}^{Z,z} = q_{nl}^{H,H} \frac{0.106}{T_i^{1/2}} \frac{Z_{eff}}{Z^2} N_e \tag{3.14}$$

With T_i now in keV. $q_{nl}^{H,H}$, on its part, refers to the l-mixing rate for two ions of Hydrogen colliding. To calculate so, the expression (3.10) has been recalled for $N_e =$

$10^4 cm^{-3}$ and $T = 1eV = 11604525.0061657K$. It has been determined for every l in each of the studied CX reactions.

Z_{eff}, is the effective charge. This means the average charge of the ions present in plasma. It simplifies the characterization of the collective behaviour of such ions. It does as well, include the ionization states and the distribution of ion charges within the plasma. Z_{eff} can be expressed as:

$$Z_{eff} = \sum_z N_z z^2 / N_e \tag{3.15}$$

As one can see, Z_{eff} depends on the ion density, N_z, one wishes to obtain once the effective emission rate is finally determined. However, for the effective emission rate to be calculated, l-mixing rate is needed and so Z_{eff} as well. Thus, this suppose a puzzle that must be somehow solved. Thanks to the assist of Dr. Dux and Dr.Mcdermott, authors of the paper "Evaluation of impurity densities from charge exchange recombination spectroscopy measurements at ASDEX Upgrade" [1], we know that the way to get Z_{eff} is by doing some approximations. One must first consider CXRS measurements for many elements. Then, a extent range of Z_{eff} values must be as well considered when analysing the data. A value of Z_{eff} is guessed in order to obtain a first result of the ion density for every element. By using such densities, a new Z_{eff} can be calculated and redo the same analysis once again so that one can finally obtain an accurate set of Z_{eff} and N_z for every measurement. Despite the fact that l-mixing affects our measurements, to a greater or lesser extent depending on the density of plasma, for the conditions that are often found in it, as it is the case we study, l-mixing must not be ignored. In fact, the l levels are mixed collisionally when:

$$A^Z_{nl} \tau^Z_{nl} \gtrsim 1 \tag{3.16}$$

where

$$A^Z_{nl} = Z^4 A^H_{nl} \tag{3.17}$$

$$(\tau^Z_{nl})^{-1} = \sum_z N_z q^{Z,z}_{nl} \tag{3.18}$$

Being A_{nl}^{Z} the total spontaneous emission rate from the n,l level. [29]

Since same data as in figure 3.1 is being used, where $Z_{eff} = 2$, it is this value the one that will be considered for our calculus.

Nonetheless, when trying to obtain the results by applying the presented expressions, a major problem is found. The orders of magnitude do not match the expected ones. For instance, for CVI, we get l-mixing rates for the studied temperatures, $n = 6$ and $l = 0, 1, 2, 3, 4, 5$ of an order between 10^{-1} and 10^{-3}, while the CX effective emission rates are between 10^{-13} and 10^{-9}. Since we are supposed to add the l-mixing rates to the effective emission rates, such results for l-mixing do not seem to be right. Every expression has been applied as explained in [29], respecting the demanded units and values. Other studies [1] have calculated the l-mixing rate by making use of the codes in OpenAdas [32]. However, this codes are currently not available for us at University of Sevilla. An specific authorization is needed in order to have access. In fact, such authorization was asked to The Adas Project in order to compare our script with theirs but the email has not been answered yet. We are now studying why our results do not fit with the calculations obtained with ADAS in [1]. For this reason and for not being able to find a solution in short time, we decided to finally not apply l-mixing rates. Yet, the theory behind the model should be the one introduced. We believe that perhaps, there must be an error in the demanded units behind the model or some concreted values that are not specified. It could be as well, that we are misunderstanding some information or making mistakes we could not realize about.

Since as one can see, if the main used expression (3.18) is presented after calculating (3.10), there is no obvious way results of the desired order of magnitude can be acquired when for $q_{nl}^{H,H}$, temperature in kelvin must be considered and for expression (3.18) temperature is squared root dividing in keV.

$$q_{nl}^{Z,z} = q_{nl}^{H,H} \frac{0.106}{T_i^{1/2}} \frac{Z_{eff}}{Z^2} \tag{3.19}$$

On its part, for the same case of $l = 0, 1, 2, 3, 4, 5, 6$, for $l = 6$ as an specific example, the resulting $q_{nl}^{H,H} = 2.81$ is obtained under the conditions in "Pengelly and Seaton" [31].

For this specific value, if we would calculate $q_{nl}^{Z,z}$ for a temperature of $1kev$, $Z_{eff} = 2$ and for Carbon VI with $Z = 6$ we can see as it follows what the result would be:

$$q_{nl}^{Z,z} = 2.81 \frac{0.106}{1^{1/2}} \frac{2}{6^2} = 0.0165 \tag{3.20}$$

As mentioned, such result (3.19) can not be applied to our data as it is significantly higher than the calculated effective emission rates.

Then, the graphics in Figure 3.1 can not be completely achieved. However, results for every effective emission rates of orders of magnitude in the same ranges as in Figure 3.1 are achieved. In the results only l-mixing is missing, which should solve the differences with Figure 3.1. The code can then give an idea of the effective emission rates one can obtain for every CXRS reaction, though they are still not completed. A new path for future works opens: trying to solve for l-mixing and adding so to the effective emission rates, as well as comparing our code with the ADAS codes when an access authorization is received.

3.3 Identifying the most convenient CXRS reaction for SMART

The SMART tokamak will be working under lower temperatures than the ones studied in [1]. In figure 3.6 a representation on the expected electron and ion temperatures against the magnetic coordinate ρ_{tor} is shown. Thus, CXRS reactions studied for writing our code in the previous sections, might not be the most suitable ones for SMART, since they consider fully ionized impurities that may not be present in SMART. Due to the low initial temperatures in SMART, non completely ionized impurities are more convenient.

SMART will count as well on Carbon limiters. A limiter has the purpose of bounding the plasma inside the tokamak. It is merely a material surface that limits the edge of plasma avoiding the contact between it and the tokamak vessel. The limiter plays an important role when protecting the walls from the plasma when instabilities occur [13].

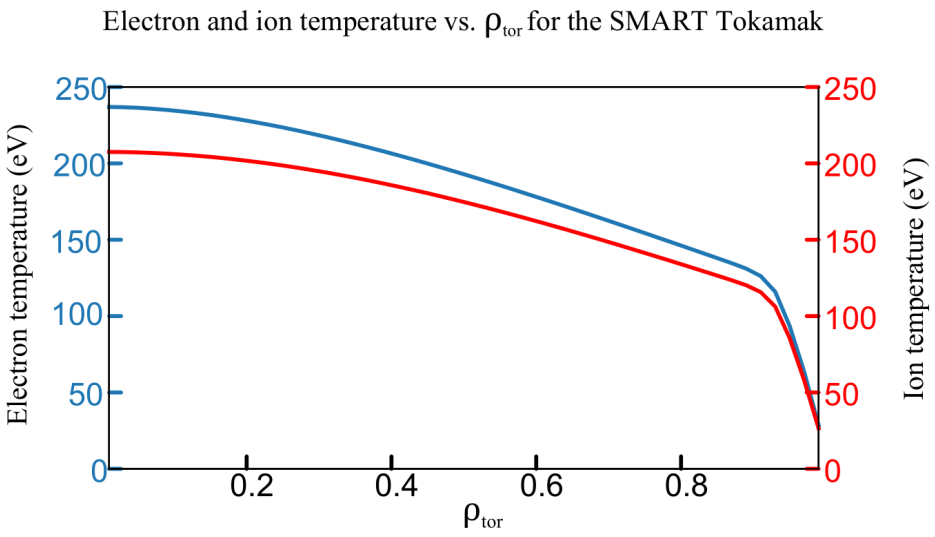

Figure 3.6: Electron and ion temperature against ρ_{tor}. Source: [33]

Moreover, in CXRS, charge exchange will occur with an ion from the limiter material as these limiters will act as a source of impurities that can be measured. This is, the injected deuterium ion will exchange an electron with an ion from the limiter and so with an ion of carbon. Such carbon ions can propagate through the entire plasma making CXRS measurements possible along the whole plasma radius. Yet, only edge measurements will be obtained due to the low penetration of the gas puff neutrals.

For such conditions in SMART, C^{2+}, seems to be a promising receiver particle for CXRS reaction since it has a proper ionization energy as we need it to be low. C^{2+} has an ionization energy of $24.38332eV$. This is the energy to remove a second ion from the C^{1+} ion.

One shall not make a direct use of our code to study CX effective emission rates for C^{2+} and deuterium for the code is missing l-mixing rates and the results would not be complete. Nonetheless, one can attempt to select which emission line of C^{2+} is the most suitable one considering the diagnostic requirements. Since in nuclear fusion it is common to use optical systems that work in the visible range of wave lengths, in order to be able to measure the reaction, we must consider one that happens in such range. This is between 380 to 750 nm. In the database NIST [34], one can find the reference for "Selected tables of atomic spectra" [35], where different ions of Carbon are found. There

one can identify that C^{2+} has a line in the spectrum on $464.7nm$ which is in the visible range. However, if in the future we are able to develop a code that can add the l-mixing effect, the effective emission rates for this ion could be analysed and prove whether it is suitable for CXRS SMART under the working temperatures or not.

4 Conclusions and future work

After introducing the theory and main concepts of nuclear fusion and tokamaks, one of the main systems for plasma diagnosis has been presented: charge exchange recombination spectroscopy (CXRS). One of the main goals of this bachelor thesis was to study CXRS effective emission rates for different CXRS reactions. With this objective, a code written in Python must be developed in order to transform raw CXRS cross-sections to effective emission rates while taking into account two different effects: nl-cascade and l-mixing. Besides, the most suitable CXRS reaction for the SMART tokamak will be as well studied.

Regarding the results of this thesis, first, a code in Pyhton has been developed that allows to read the atomic data for every CX reaction from the database OpenAdas. Next, a code that calculates effective emission rates for different CX reactions has been written. To make sure that the code works properly, the same results for effective emission rates as in the paper "Evaluation of impurity densities from charge exchange recombination spectroscopy measurements at ASDEX Upgrade" [1] were attempted to be reproduced. Effective emission rates from raw cross-sections were successfully obtained by using the Maxwellian distribution. Next, the nl-cascade process has been taken into account. The nl-cascade rate has been determined for each of the studied reactions. A comparison between the results for effective emission rates with and without nl-cascade effect is also shown for the specific case of CVI as an example.

However, the resulting effective emission rates are missing the l-mixing corrections [29]. It should be included in the calculation as it is an important rate that should solve the differences between our results and the reference followed in this work. Nonetheless, as indicated in the previous chapter, the results do not have the proper orders of

magnitude even though the calculations have been followed as explained in [29]. In collaboration with researchers from the Max Planck Institute, no obvious mistake was identified. A comparison of our working method with the code available in ADAS is pending and will be carried out as soon as the authorization to the ADAS environment is granted by its developers. Yet, for the effective emission rates, we obtain similar orders of magnitude as the referenced paper. The differences should only lie on not adding the l-mixing rates. Meanwhile, results for effective emission rates for every studied CXRS reaction are obtained in the same range of orders of magnitude as in [1]. Hence, with the code it is still possible to get an accurate idea of the CXRS effective emission rates for different temperature values and energies.

In order to identify a suitable reaction for CXRS at SMART, a study on the ionization energy and wave-length range for different ionization stages of carbon has been done, as the limiters in the SMART tokamak will be made out of carbon. This was the second objective of this bachelor thesis. C^{2+} seems to be a promising candidate because of its low ionization energy and a specific line in the visible wavelength range. For these reasons C^{2+} has been identified as a good option.

A new possible path for future projects opens: being able to complete the calculation on l-mixing rates without making use of OpenAdas codes in order to have a complete code. Once the script works as wished, one can obtain the effective emission rates for any receiver and donor ion. This way one is able to study if the reaction with C^{2+} is really suitable for CXRS at SMART by looking at its CXRS effective emission rates for low temperatures. The code was written and used for specific data but it can be used for any reaction. It is developed in a general way so that it is easy to change the parameters and the reactions in order to get different results. Thus, once l-mixing would be added, it could be considered as a versatile tool to calculate the CXRS effective emission rates needed for the impurity density evaluation.

Bibliography

[1] R. M. McDermott; et al. “Evaluation of impurity densities from charge exchange recombination spectroscopy measurements at ASDEX Upgrade”. In: *Plasma Physics and Controlled Fusion* (2018). DOI: 10.1088/1361-6587/aad256.

[2] J. Lelieveld et al. “Effects of fossil fuel and total anthropogenic emission removal on public health and climate”. In: *Proceedings of the National Academy of Sciences* (2019). DOI: 30910976.

[3] Our world in data. *CO2 by fossil fuels*. www.ourworldindata.org/emissions—by—fuel. 2022.

[4] Our world in data. *Years of fossil fuels reserves left*. www.ourworldindata.org /grapher/ years-of-fossil-fuel-reserves-left. 2022.

[5] Our world in data. *Global energy consuption from 1940 to 2021*. www.ourworldindata.org/energy-production-consumption. 2022.

[6] C. Stern. CNN. *Germany closes its last nuclear power plants*. www.edition.cnn.com /2023/04/15/europe /germany-nuclear-phase -out-climate-intl/index. 2023.

[7] Ministery for the environmental transition and demographic challenge. Spanish Government. *Spanish national climate plan*. www.miteco.gob.es/planes-estrategias /plan- nacional-integrado energiaclima/ plannacionalintegradodeenergiayclim a 2021-2030. 2020.

[8] J. O. Engler. “Global and regional probabilities of major nuclear reactor accidents”. In: *Journal of environmental management* (2020). DOI: 10.1016/j.jenvman.2020.110780.

[9] World Nuclear Association Conference. "World Nuclear Performance Report 2022". In: 2022.

[10] Science Learning Hub. *Proton-proton fusion*. www.sciencelearn.org.nz/images/244-proton-proton-chain-reaction. 2014.

[11] G. Khatri. *Master Thesis: Toroidal Equilibrium Feedback Control at EXTRAP T2R*. 2010.

[12] H. Matsumoto et al. "Health effects triggered by tritium: how do we get public understanding based on scientifically supported evidence?" In: *Journal of radiation research* (2021). DOI: 62(4):557âĂŞ563.

[13] J. Wesson and D. J. Campbell. *Tokamaks*. Oxford science publications, 2004. ISBN: 9780198509226.

[14] IAEA. *Conventional tokamak*. www.iaea.org/es/ energia-de-fusion /fusion-por- confinamiento -magnetico-con-tokamaks. 2022.

[15] G. Witvoet. "Conference Talk: Modeling and simulating the sawtooth instability in nuclear fusion". In: 2009.

[16] ITER organization. *Q maximum acchieved by JET*. www.iter.org/sci/BeyondITER. 2023.

[17] S. E. Wurzel and S. C. Hsu. "Progress toward fusion energy break even and gain as measured against the Lawson criterion". In: *AIP Publishing. Physics of plasma* (2022). DOI: 062103.

[18] E. Viezzer et al. "La fábrica de estrellas en la tierra: El tokamak SMART de la Universidad de Sevilla". In: *university of Sevilla* (2022).

[19] Z. Gao. "Compact magnetic confinement fusion: Spherical torus and compact torus". In: *Matter and Radiation at Extremes* (2016). DOI: 10.1016/j.mre.2016.05.004.

[20] P. T. Lang et al. "ELM control strategies and tools: status and potential for ITER". In: *Nuclear Fusion. IAEA* (2013). DOI: 10.1088/0029-5515/53/4/043004.

[21] F. Ryter et al. "Expression for the Thermal H-Mode Energy Confinement Time under ELM-free Conditions. Max-Planck-Institut für Plasmaphysik, Garching (DE)". In: *Nuclear Fusion. IAEA* (1193). DOI: 24071009.

[22] R. M. McDermott; et al. “Edge radial electric field structure and its connections to H-mode confinement in Alcator C-Mod plasmas”. In: *AIP Publishing. Physics of plasma* (2009). DOI: 056103.

[23] Columbia Plasma Physics Lab. *Plasma triangularity*. www.plasma.apam.columbia.edu/news/columbia-engineering-students-win- fusion-energy-design-contest. 2023.

[24] The Adas Project. *OpenAdas database*. https://open.adas.ac.uk/. 1195-2023.

[25] D. J. Cuz-Zabala et al. “Upgrade of the edge Charge Exchange Recombination Spectroscopy system at the High Field Side of ASDEX Upgrade”. In: *Journal of Instrumentation* (2019). DOI: 10.1088/1748-0221/14/11/C11006.

[26] RP Photonics AG. *Doppler broadening*. www.rp-photonics.com/dopplerbroadening.html. 2021.

[27] K. Igenbergs et al. “Charge exchange and ionization in N7 +−, N6 +−,C6 +−H(n = 1, 2) collisions studied systematically by theoretical approaches”. In: *Journal of Physics B: Atomic, Molecular and Optical Physics* (2012). DOI: 10.1088/0953-4075/45/6/065203.

[28] R. M. Churchill et al. “Development of the gas puff charge exchange recombination spectroscopy (GP-CXRS) technique for ion measurements in the plasma edge”. In: *Review of Scientific Instruments* (2013). DOI: 10.1063/1.4821084.

[29] R. J. Fonck et al. “Determination of plasma-ion velocity distribution via charge exchange recombination spectroscopy”. In: *Phys. Rev. A* (1984). DOI: 10.1103/PhysRevA.29.3288.

[30] K. Omidvar; NASA. “Tables of transition probabilities and branching ratios for electric dipole transitions between arbitrary levels of Hydrogen−like atoms”. In: *Atomic Data and Nuclear Data Tables* (1980). DOI: 10.1016/0092-640X(83)90011-6.

[31] R. M. Pengelly and M. J. Seaton. “Collisional transitions between states of degenerate energy levels (II)”. In: *Monthly Notices of the Royal Astronomical Society* (1964). DOI: 10.1093/mnras/127.2.165.

[32] The Adas Project. *Manual for ADAS314: Convert QCX to effective cross sections*. 2022.

[33] A. Mancini et al. “Predictive simulations for plasma scenarios in the SMART Tokamak using ASTRA and ASCOT5. SOFT conference”. In: 2022.

[34] NIST ASD team. *NIST databse*. www.nist.gov/pml/atomic-spectra-database. 1995-2022.

[35] C. E. Moore. *Selected tables of atomic spectra*. NBS publications, 1970. ISBN: ADD095234.